communications physics

A Nature Portfolio journal

Article

Article in Press

https://doi.org/10.1038/s42005-026-02813-2

Exciton dynamics in monolayer WSe_2 probed by ultrafast valley-selective second-harmonic microscopy

Marleen Axt[1,4], Benjamin G. Whetten[2,4], Gerson Mette[1], Jens Güdde[1], Markus B. Raschke[2] ✉ & Ulrich Höfer[1,3] ✉

The broken inversion symmetry and strong spin-orbit coupling of transition metal dichalcogenides and the resulting spin-valley locking are the foundation for potential two-dimensional spin devices and valleytronics. However, ultrafast valley polarization is difficult to characterize due to the need to image both intra- and inter-valley scattering across the Brillouin zone. Here, we present an all-optical method for measuring the rate of ultrafast spin- and momentum-conserving scattering through circularly-polarized time-resolved pump-probe second-harmonic spectroscopy. With Wollaston-prism-based detection for facile and simultaneous measurement of both K and K' valley populations, using the example of exfoliated tungsten diselenide monolayers we resolve intra-valley and inter-valley scattering rates of 460 fs and 20 fs, respectively. These ultrafast time scales indicate rapid room-temperature valley depolarization through either intervalley exchange coupling or the Elliot-Yafet mechanism, and are consistent with recent time-resolved molybdenum diselenide and tungsten disulfide results.

Transition metal dichalcogenide (TMD) monolayers have attracted considerable interest due their direct band gap at the K points of the Brillouin zone[1] and strong exciton binding energies due to reduced electronic screening[2] with promising optoelectronic applications[3–5], including twisted Moiré-physics-based devices[6]. Broken inversion symmetry and strong spin-orbit coupling make TMDs unique among the expanding list of 2D materials by coupling the electron spin to the valley pseudospin, resulting in spin-split valence and conduction bands at the K valley, with opposite orientation at the K' valley. This spin-split band structure allows formation of what are known as A and B-excitons at the K and K' points, with an excited electron bound to a hole in the upper or lower valence band, respectively. The strong spin-orbit coupling enables valley specific optical excitation of both A and B-excitons, forming the basis of proposed valleytronics for information processing and storage in this new valley degree of freedom[3,7].

Although the large exciton binding energies in TMDs preserve these unique optical properties at room temperature, their practical application crucially depends on the lifetime of the optically generated valley polarization, which can be lost by exciton transfer from the K to K' point due to intervalley exchange coupling (IEC), where electrons and holes flip their spin simultaneously[8–12]. In addition, the lifetime of the valley polarization is also limited by scattering with phonons, defects, or impurities, including both spin-conserving and non-spin-conserving scattering events through the Elliot-Yafet (EY) mechanism[13–15]. Both IEC and EY phonon scattering result in a redistribution of the initial spin-selective excitation in the Brillouin zone, forming excitons with non-zero center-of-mass momenta (momentum-dark excitons) and excitons with opposite spin states of electron and hole (spin-dark excitons)[15,16].

Early valley polarization models estimated valley-spin lifetimes of nanoseconds[17]. However, later studies found that valley depolarization occurs on the scale of hundreds of fs at room temperature due to rapid IEC, EY phonon scattering, and coupling to dark exciton states[9,12,15]. A robust model of valley depolarization on the fs scale requires measurement of the intervalley and intravalley scattering rates and careful monitoring of both the K and K' valley populations. Previous measurements of valley polarization have used circularly polarized photoluminescence[17,18], absorption spectroscopy[19], or second-harmonic spectroscopy[20,21], yet lacked the necessary temporal resolution and valley polarization sensitivity to fully characterize both spin- and momentum-forbidden scattering pathways.

Previously, we demonstrated that second-harmonic pump-probe spectroscopy can resolve ultrafast carrier dynamics in 2D materials with 10 fs resolution by measuring twist-angle-dependent charge transfer times as short as 12 fs in MoS_2/WSe_2[22] and $MoSe_2/WSe_2$[23] heterobilayers. In an

[1]Department of Physics, Philipps-University of Marburg, Marburg, Germany. [2]Department of Physics, University of Colorado, Boulder, CO, USA. [3]Department of Physics, University of Regensburg, Regensburg, Germany. [4]These authors contributed equally: Marleen Axt, Benjamin G. Whetten.
✉e-mail: markus.raschke@colorado.edu; hoefer@physik.uni-marburg.de

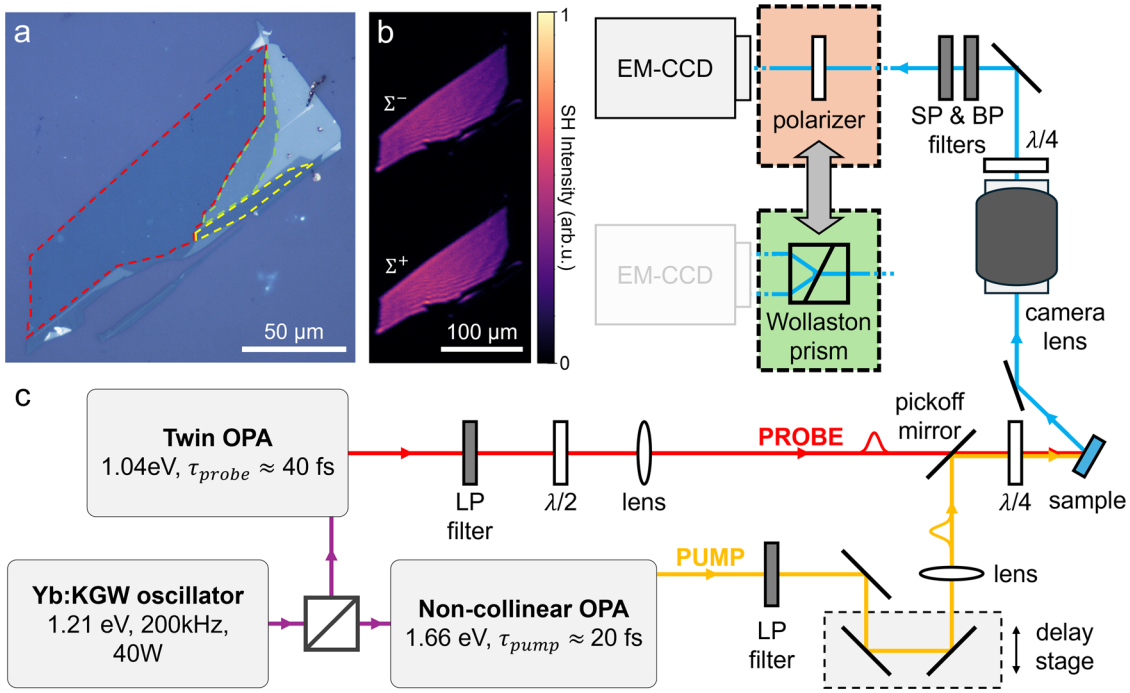

Fig. 1 | Optical layout for ultrafast spin-selective second-harmonic spectroscopy. **a** White light microscope image of a WSe_2 flake with monolayer (red), bilayer (yellow), and trilayer (green) regions outlined. **b** image of both second-harmonic polarizations, spatially separated with the Wollaston prism, showing strong signal from mono- and trilayer, but not bilayer regions. **c** Ultrafast second-harmonic generation (SHG) microscope layout for circularly polarized SHG pump-probe detection with single polarization detection (red box) and simultaneous dual-polarization detection (green box).

extension of that same ultrafast pump-probe technique, now with valley selectivity, we present a method of ultrafast pump-probe second-harmonic micro-spectroscopy which enables the simultaneous tracking of both the K and K' valley populations and ultrafast valley polarization dynamics in 2D materials. In this all-optical technique, applied here to a WSe_2 monolayer, we resonantly excite 1 s A excitons with a valley-selective circularly polarized pump pulse. We then probe the valley polarization with a linearly polarized probe pulse tuned close to half the energy of the 1 s B exciton energy, generating resonant second-harmonic generation (SHG) emission.

Significantly, we implement a two-channel parallel detection scheme in which the two opposite helicity components of the probe fundamental and its second-harmonic (SH) are spatially separated by a combination of a λ/4-plate and a Wollaston prism, enabling simultaneous measurement of both valley polarizations. We find distinctly different dynamics for probing the 1 s B exciton in the same vs the opposite valley with respect to the initial pump polarization, which we interpret as the fast formation of momentum-dark excitons followed by the slower formation of spin-dark excitons. Ultrafast second-harmonic pump-probe spectroscopy, as demonstrated here, complements recent time-resolved and angle-resolved photoelectron spectroscopy (tr-ARPES) studying ultrafast valley depolarization and scattering across the Brillouin zone[24,25].

Method

All measurements were performed under ambient conditions with a specially designed ultrafast pump-probe SHG microscope in reflection geometry as illustrated in Fig. 1. A Yb:KGW-based laser (Carbide, Light Conversion, 220 fs pulse duration, 200 kHz repetition rate) pumps two optical parametric amplifiers (OPA). The first is a non-collinear OPA (Orpheus-N, Light Conversion) which provides ~20 fs pump pulses tuned to the 1 s A exciton resonance of WSe_2 at 1.66 eV (λ = 745 nm). The other (Orpheus-F Twin, Light Conversion) consists of two hybrid collinear/non-collinear OPAs, providing ~40 fs probe pulses tuned to 1.04 eV (λ = 1192 nm), close to half of the 1 s B exciton resonance energy. The time-delay between pump and probe pulses is controlled by a motorized delay stage. A combination of a λ/2-plate and a polarizer is used to control the pulse power of each laser beam. Low-pass filters are used to block residual short wavelength contributions in the incident beams to minimize the background in the detected second-harmonic signal. The pump and the probe beams are slightly focused by thin fused-silica lenses with focal lengths of 50 cm. Both beams are combined collinearly by a pickoff mirror, steering the combined beam pair through a broadband λ/4-plate (RAC 5.4, Bernhard Halle Nachfl., 600–1200 nm) onto the sample at an angle-of-incidence of ~5°. The helicity of the circularly polarized pump beam is solely controlled by this λ/4-plate, while the helicity of the probe beam can be varied independently by an additional λ/2-plate in the probe path. The sample is placed slightly in front of the focus, with pump and probe beam spots on the sample being elliptical, with 485 μm and 380 μm major and minor diameters for the probe beam, and 240 μm and 210 μm for the pump beam.

Typical fluence values used were 200 μJ · cm^{-2} and 1 mJ · cm^{-2}, respectively for pump and probe, corresponding to exciton densities of approximately $10^{13}/cm^2$ using established absorption values[26], and below the Mott transition at $10^{14}/cm^2$[27]. The SHG signal is collected by a camera lens (Nikkor 50 mm 1.4 AIS, Nikon) in specular direction and imaged on an electron-multiplied charged-coupled device (CCD) (ProEm-HS, Princeton Instruments ProEM-HS) with typical exposure times of 10 s. A combination of two 600 nm band-pass filters (Semrock) together with a 650 nm shortpass filter (Thorlabs, FESH0650) is used to block the the pump and probe light as well as the second-harmonic of the pump light at 373 nm but transmit the second-harmonic of the probe pulses at 596 nm. With a magnification of M ≈ 38, an area of about 350 × 350 $μm^2$ of the sample can be imaged with a spatial resolution better than 2 μm. While both monolayer and trilayer regions demonstrate strong second-harmonic response (Fig. 1b), for pump-probe measurements the SH signal is spatially integrated over the monolayer region of interest (Fig. 1a, red outline) to isolate the monolayer response.

A parallel detection scheme is then used in which the probe fundamental is linearly polarized and the two opposite helicity components of its second-harmonic are spatially separated by a combination of a second λ/4-plate (RAC 5.4, Bernhard Halle Nachfl., 600–1200 nm) and a Wollaston prism in front of the CCD, with a resulting divergence of 0.5°. In this way,

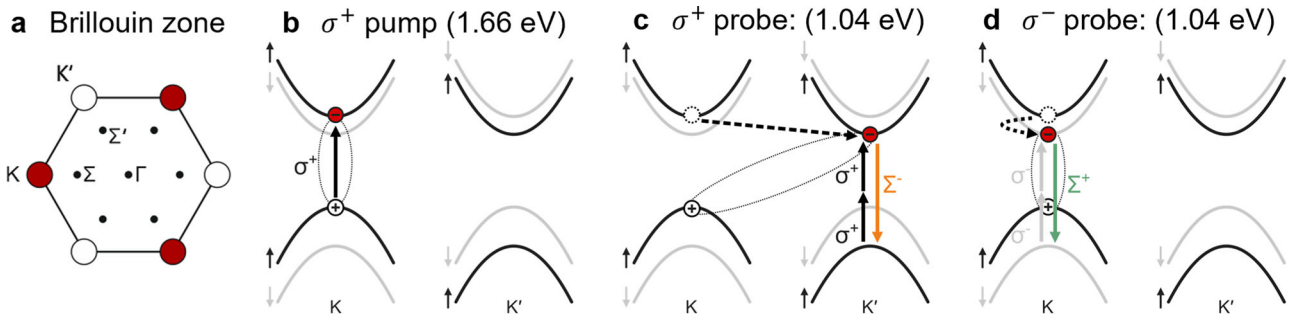

Fig. 2 | Band structure of monolayer WSe_2. **a** Brillouin zone of WSe_2 with its high symmetry points. **b** Resonant excitation of A excitons selectively at the K points by left circularly polarized (σ^+) pump pulses. **c** Selective right circularly polarized (Σ^-) SHG-probe of B excitons at the K' points with left circularly (σ^+) polarized probe pulses tuned to half of the B exciton excitation energy. **d** Selective left circularly polarized (Σ^+) SHG-probe of B excitons at the K points with right circularly (σ^-) polarized probe pulses. (Band gap energy and spin-splitting not to scale).

two laterally shifted replica of the SHG image of opposite helicity can be recorded simultaneously. The resulting lateral separation on the recorded image amounts to about 50% of its side length. This detection scheme provides negligible crosstalk between the spatially separated images in the case of isolated optically active flakes on an optically inactive substrate. In addition to reducing measurement time, it guarantees that the two spatially resolved SHG transients for the two opposite helicities are recorded for identical delays, which eliminates temporal shifts of the transients between sequential delay scans.

For comparison, a sequential detection scheme is also used where the helicity of the detected second-harmonic is selected by a combination of a $\lambda/4$-plate and a polarizer (LPVISE100-A, Thorlabs, 400–700 nm) in front of the CCD. In this way, spatially resolved SHG transients for the two different helicity combinations of the probe fundamental and its second-harmonic σ^+/Σ^- and σ^-/Σ^+ are recorded sequentially. The resulting time-dependent transients were fit to a valley depolarization model as described in Results and Discussion using a least squares regression in Python.

ML WSe_2 samples were prepared on PDMS (dimethylpolysiloxane) by mechanical exfoliation from a bulk single crystal (HQ Graphene) and identified through micro-photoluminescence of the characteristic direct band gap A excitons at 1.66 eV, using 445 nm laser excitation. The monolayer flakes were then transferred onto a SiO_2/Si(001) substrate with 100 nm oxide film thickness.

Results and discussion

The valley-selective excitation by circularly polarized pump light is based on the selection rules for optical dipole transitions together with the coupling of spin and valley degree of freedom in monolayer TMDs of D_{3h} symmetry with reduced local C_{3h} symmetry at the K and K' points[28,29]. These conditions specify that a single-photon transition at the 1 s A exciton resonance with left (right) circularly polarized light, denoted by σ^+ (σ^-), predominantly generates 1 s A excitons in the K (K') valleys as illustrated in Fig. 2b. By extending the optical selection rules to multi-photon dipole transitions, it has been shown that a two-photon excitation near the K (K') points of monolayer TMDs with local C_{3h} symmetry require two σ^- (σ^+) circularly polarized photons that may generate one left (right) circularly polarized photon at the SH frequency, denoted by Σ^+ (Σ^-)[30] (Fig. 2c, d). Through two photon resonance, SHG is resonantly enhanced when the probe photon energy is tuned to half the 1s B-exciton energy[20]. Therefore, SHG from left (right) circularly polarized probe photons with this choice of photon energy selectively probes bright 1s B-excitons at the K (K') points (Fig. 2c, d). Additionally, with the probe photon energy far from any single-photon resonance, electron population in the conduction bands induced by the probe pulses that may interfere with the excited electron population induced by the pump pulses can be neglected.

Figure 1a shows a white light image of a WSe_2 sample with both mono- and multi-layer regions, with Fig. 1b showing the two SHG images of the same sample obtained simultaneously by the dual channel SH imaging corresponding to the σ^+ and σ^- probe polarizations. The monolayer region stands out due to its strong SH response, with negligible multilayer or SiO_2/Si(001) substrate response. The SH intensities from the monolayer for the two different probe polarizations are almost identical. This shows that the SH probes the $K^{\downarrow}$ and $K'^{\uparrow}$ bands symmetrically.

After validating the expected symmetry selectivity of the SH response in static SHG imaging we perform pump-probe spectroscopy to resolve the underlying dynamics of intra- and inter-valley scattering. Figure 3 shows the resulting temporal response of the SH intensity from the 1.04 eV probe integrated over the WSe_2 monolayer region following excitation of the 1 s A excitons at the K point with a left (σ^+) circularly polarized 1.66 eV pump pulse.

Considering that the dependence of the SH response on the excited carrier population near an exciton resonance is generally complex, owing to competing effects such as Pauli blocking, band-gap renormalization, and interference between resonant and non-resonant contributions to the nonlinear susceptibility $\chi^{(2)}$, we performed pump-fluence-dependent measurements to confirm that the second-harmonic response of the probe increases approximately linearly with pump fluence over the range used here (Fig. 3c, inset)[31]. Therefore, regardless of the origin of the pump-induced increase in SHG, the small magnitude of the signal change ($\lesssim$20%) and its approximately linear fluence dependence allow us to use the transient SHG signal as a proxy for the relaxation dynamics of the excited carrier population. We note that, although the probe spectral bandwidth (~100 meV FWHM) is larger than the conduction band spin-splitting at the K and K′ points (~50 meV), contributions from the $K^{\uparrow}$ and $K'^{\downarrow}$ bands to the circularly polarized resonant SH response are expected to be negligible compared to $K^{\downarrow}$ and $K'^{\uparrow}$ due to spin-valley locking.

Thus, the left (σ^+) circularly polarized probe component generates right (Σ^-) circularly polarized SHG that probes excited carriers in the $K'^{\uparrow}$ band (Fig. 3b, c, orange), while the right (σ^-) circularly polarized probe component generates left (Σ^+) circularly polarized SHG that probes excited carriers in the $K^{\downarrow}$ band (green). The two transients show distinctly different dynamics. Probing with a $\sigma^+/\sigma^+\Sigma^-$ polarization combination results in a fast rise of the SH intensity with a peak at around ~100 fs and a subsequent slower decrease towards a plateau for delay times $\gtrsim$ 400 fs. In contrast, the SH intensity for probing with a $\sigma^+/\sigma^-\Sigma^+$ polarization combination rises more slowly but recovers and plateaus with similar dynamics as the slow component of the signal for probing with σ^+ polarization. Both signals show slight oscillations with periods of $\lesssim$100 fs due to coherent exciton-phonon scattering[32] and slowly decay on much longer timescales (not shown) to the initial SH values observed at negative delay times. The distinctly different dynamics between the two transients clearly show that opposite circular probe polarizations probe different processes.

We interpret these distinct dynamics as follows. Initially excited 1s A excitons at the K(K') points in WSe_2 consist of an electron and a hole with the same spin orientation in the respective energetic upper of the spin-split conduction and valence bands (Fig. 2b)[8,17,33,34]. Consequently, the

corresponding band of the same spin orientation in the K'(K) valleys is the lower one with respect to a negatively charged electron and the upper one with respect to the positively charged hole. It is therefore energetically neither favorable that the holes scatter into the lower valence band of the K(K') valleys nor into that of the K'(K) valleys. We therefore assume in the following that the holes remain in the upper spin-split valence band of the initially excited K(K') valleys. This would leave excited electrons that can lose their energy by scattering to the lower conduction band of either the K'(K) valleys (Fig. 2c) or the initially excited K(K') valleys (Fig. 2d) forming either momentum-dark KK'(K'K) or spin-dark KK(K'K') excitons, respectively. Since both spin- and momentum-dark excitons as well as bright 1 s B excitons are formed from electrons in the lower conduction band, the transient change of the detected Σ^+ (Σ^-) circularly polarized SHG after excitation of 1 s A excitons at K should reflect the formation dynamics of spin(momentum)-dark excitons. Because the formation of spin-dark excitons requires spin-flip scattering, we can expect it to proceed on a longer time scale compared to the formation of momentum-dark excitons. Both types of scattering may proceed via different pathways through the Brillouin zone including other high-symmetry points (Fig. 1a), in particular the $\Sigma(\Sigma')$ points[15], which we do not monitor in this experiment.

In addition, exciton transfer between valleys without energy loss can be mediated by intervalley exchange coupling (IEC) through dipole-dipole interactions[8–12]. However, theoretical calculations suggest that the IEC efficiency is suppressed in tungsten-based TMDs, in particular at room temperature, due to the fast formation of momentum-dark excitons by phonon-meditated scattering of the electron from the K(K') to the $\Sigma(\Sigma')$ and the K'(K) points[15]. Theoretical studies have instead predicted that the EY mechanism may dominate the rapid loss of valley polarization at room temperature through non-spin-conserving scattering events[13,14]

In order to fit the data we apply a model of momentum and spin-flip scattering to obtain estimates for these scattering times. To restrict the number of free parameters, we consider only four different exciton populations: the population $N_K^{\uparrow}$ of the initially excited bright $K^{\uparrow}K^{\uparrow}$ excitons, the population $N_K^{\downarrow}$ of spin dark $K^{\uparrow}K^{\downarrow}$ excitons, the population $N_{K'}^{\uparrow}$ of momentum dark $K^{\uparrow}K'^{\uparrow}$ excitons, and the population $N_{K'}^{\downarrow}$ of momentum- and spin-dark $K^{\uparrow}K'^{\downarrow}$ excitons. By assuming that the pump-induced change of the SH intensity for $\sigma^+(\sigma^-)$ pump pulses is approximately linear with the population of momentum dark $K^{\uparrow}K'^{\uparrow}$ (spin dark $K^{\uparrow}K^{\downarrow}$) excitons, we consider the experimental time-resolved SH traces as a measure of $N_{K'}^{\uparrow}(N_K^{\downarrow})$. The scattering processes are initially described by three different rates: a rate r_q for momentum scattering between $K^{\uparrow}K^{\uparrow}$ and $K^{\uparrow}K'^{\uparrow}$ excitons that preserves the spin, a rate r_s for pure spin-flip scattering between $K^{\uparrow}K^{\uparrow}$ and $K^{\uparrow}K^{\downarrow}$ as well as between $K^{\uparrow}K'^{\uparrow}$ and $K^{\uparrow}K'^{\downarrow}$ excitons, and a rate r_{qs} for simultaneous momentum and spin-flip scattering between $K^{\uparrow}K^{\uparrow}$ and $K^{\uparrow}K'^{\downarrow}$ as well as between $K^{\uparrow}K'^{\uparrow}$ and $K^{\uparrow}K^{\downarrow}$ excitons (Fig. 3a).

The population of electrons in the four conduction bands can be described by the rate equation

$$\dot{\mathbf{N}} = \mathbf{R}\,\mathbf{N} + \mathbf{p}(t), \tag{1}$$

with population number $\mathbf{N} = [N_K^{\uparrow}, N_{K'}^{\uparrow}, N_{K'}^{\downarrow}, N_K^{\downarrow}]$, pump term $\mathbf{p}(t) = [\frac{1}{\sqrt{\pi}w} e^{-(t/w)^2}, 0, 0, 0]$, and rate coefficient matrix **R,**

with $n_K^{\uparrow}, n_{K'}^{\uparrow}, n_K^{\downarrow}$, and $n_{K'}^{\downarrow}$ as the equilibrium populations of the four conduction bands. Previous studies have demonstrated that scattering into opposite spin states occurs primary through a stepwise process of phonon-mediated formation of momentum-dark excitons $K^{\uparrow}K'^{\uparrow}$ facilitating the formation of $K^{\downarrow}K'^{\downarrow}$ excitons through IEC[12]. Thus, due to the slow rate of IEC compared to spin-conserving intervalley scattering, both r_s and r_{qs} can be approximated by a single rate of spin-flip scattering, r_s', simplifying Eq. (2) significantly. For completeness, we also include relaxation of all populations by recombination with a time constant τ, however we approximate $\tau^{-1} \approx 0$ due to $r_{q,s,qs} \gg \tau^{-1}$ and the SH signal already reaching quasi-equilibrium values for $t \gtrsim 400$ fs.

Because our experiment does not monitor exciton populations beyond the K and K' points, we do not explicitly consider the fast momentum scattering via the Σ and Σ' points[15]. Therefore, the scattering rates for scattering between the K and K' points here not only include the contribution from direct scattering between K and K' but also the contribution from scattering via other high symmetry points, in particular the Σ and Σ' points. Additionally, while this model does not explicitly account for charged exciton states, additional bound electrons and holes are expected to follow the same scattering pathways as neutral excitons and thus would not significantly modify the time-dependent response.

The normalized SH response (Fig. 3) exhibits a dip at time zero in cross-polarization while the co-polarized signal contains a similar positive coherent contribution at time zero that is partially masked by the rapid rise in signal. The modification of the SHG intensity at time zero may result from optical rectification or photocurrents from the pump pulse creating low frequency fields that give rise to an optically-generated electric field induced second-harmonic (EFISH) signal[35,36] which interferes with the SHG signal, with similar effects previously observed in semiconductor interfaces[37,38]. The degree of interference varies with pump energy, as shown in Fig. 4, eventually flipping sign when the pump energy is below the A-exciton resonance. In this case, the rapidly varying phase of the complex nonlinear susceptibility of the WSe_2 as the pump energy passes through the A-exciton resonance would modify the relative phase between the SHG and EFISH-like signals causing a transition from destructive to constructive interference. We explicitly account for this transient interference effect at time zero by adding a gaussian pulse with width fixed to the pump pulse FWHM to the fit function, and the resulting fits yield consistent scattering rates regardless of the size of the interference effect (Fig. 3).

The resulting fits to the SH signal (Fig. 3, solid lines) yield scattering rates of $r_q = (20 \pm 3)$ fs and $r_s' = (460 \pm 10)$ fs when averaged across five different measurements. These values agree remarkably well with previous results that found a room temperature intervalley scattering time of 16 fs between the K and Σ valleys in WS_2 monolayers[39] and longer spin-flip scattering times in the hundreds of fs for $MoSe_2$[12,15]. Importantly, both our σ^+ and σ^- pump polarization data result in comparable scattering rates, confirming the symmetric response of the K and K' valleys. Although we cannot distinguish between IEC, EY phonon scattering, or scattering through the Σ valley, we do observe rapid intervalley scattering at few-fs time scales leading to rapid valley decoherence in the WSe_2 monolayer for both pump polarizations.

$$\mathbf{R} = \begin{bmatrix} -(r_q + r_{qs} + r_s + \tau^{-1}) & r_q \frac{n_K^{\uparrow}}{n_{K'}^{\uparrow}} & r_{qs}\frac{n_K^{\uparrow}}{n_{K'}^{\downarrow}} & r_s \frac{n_K^{\uparrow}}{n_K^{\downarrow}} \\ r_q & -\left(r_q \frac{n_K^{\uparrow}}{n_{K'}^{\uparrow}} + r_{qs} + r_s + \tau^{-1}\right) & r_s \frac{n_{K'}^{\uparrow}}{n_{K'}^{\downarrow}} & r_{qs}\frac{n_{K'}^{\uparrow}}{n_K^{\downarrow}} \\ r_{qs} & r_s & -\left(r_q + r_{qs}\frac{n_K^{\uparrow}}{n_{K'}^{\downarrow}} + r_s \frac{n_{K'}^{\uparrow}}{n_{K'}^{\downarrow}} + \tau^{-1}\right) & r_q \frac{n_{K'}^{\downarrow}}{n_K^{\downarrow}} \\ r_s & r_{qs} & r_q & -\left(r_q \frac{n_{K'}^{\downarrow}}{n_K^{\downarrow}} + r_{qs}\frac{n_{K'}^{\uparrow}}{n_K^{\downarrow}} + r_s \frac{n_K^{\uparrow}}{n_K^{\downarrow}} + \tau^{-1}\right) \end{bmatrix} \tag{2}$$

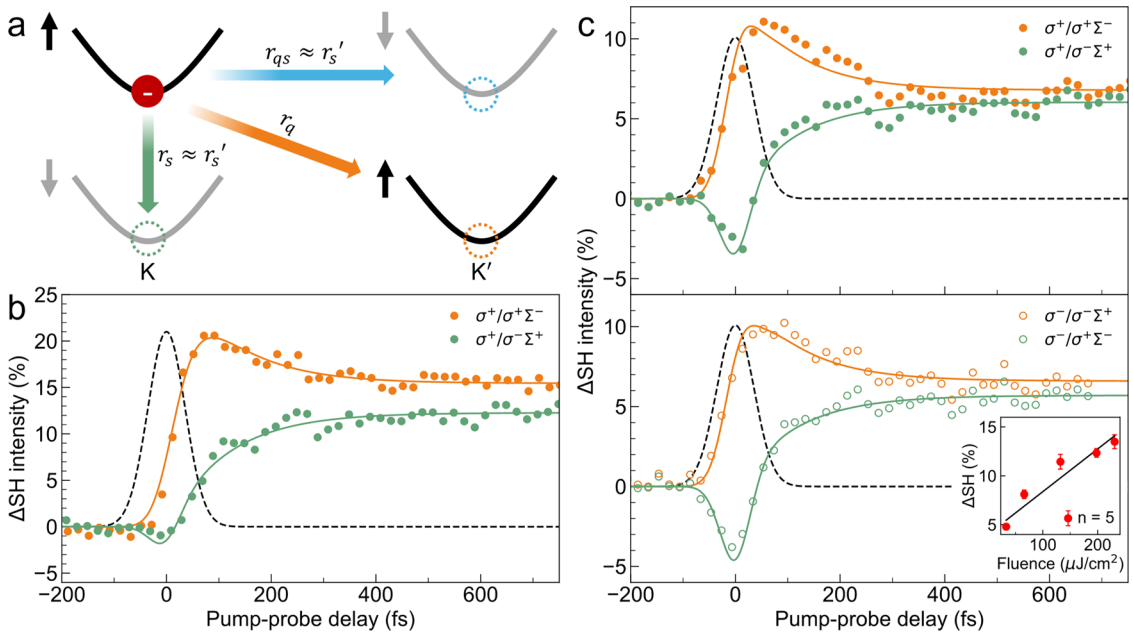

Fig. 3 | Spin-selective time-dependent second-harmonic response of monolayer WSe_2. a The 1.66 eV σ^+ circularly polarized pump selectively excites electrons into the upper conduction band at the K point, with subsequent relaxation through momentum-forbidden scattering r_q, spin-forbidden scattering r_s, or spin- and momentum-forbidden scattering r_{qs} into the other conduction bands. The 1.04 eV σ^+ and σ^- probe polarizations measure the resulting carrier dynamics in the $K'^{\uparrow}$ and $K^{\downarrow}$ bands, respectively. Both sequential (**b**) and simultaneous detection (**c**) give a similar SH response (dots) after 1.66 eV pump excitation (dashed line) which is fit (solid lines) with a coupled rate equation model (Eq. (1) and (2)), with $r_q^{\sigma+} = 32$ fs and $r_s'^{\sigma+} = 456$ fs for (b), and $r_q^{\sigma+} = 18$ fs, $r_s'^{\sigma+} = 443$ fs, $r_q^{\sigma-} = 17$ fs, and $r_s'^{\sigma-} = 503$ fs for (**c**). Inset in (**c**) shows the approximately linear trend of the change in second harmonic intensity with pump fluence for the $\sigma^+/\sigma^+\Sigma^-$ polarization combination, presented as the mean value of the maximum change in second-harmonic intensity across $n = 5$ data points plus or minus one standard deviation.

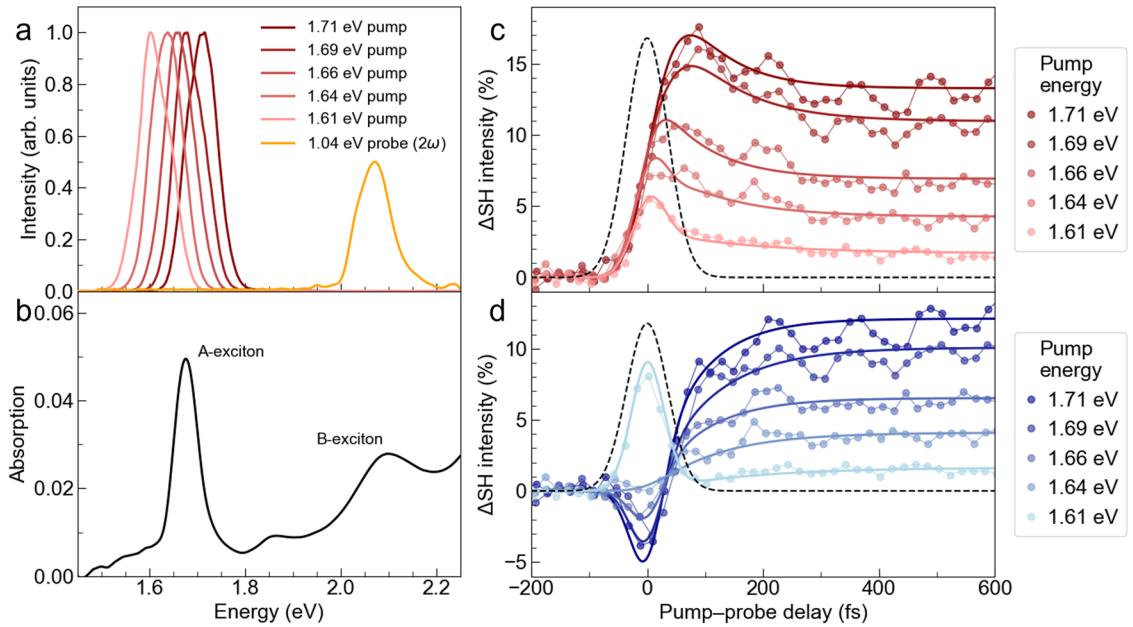

Fig. 4 | Pump pulse energy dependent second-harmonic response. a Spectra of pump fundamental (red) and frequency doubled probe (orange) overlap with the A-exciton and B-exciton absorption resonances of WSe_2, respectively (**b**). Dependence of $\sigma^+\Sigma^-$ (**c**) and $\sigma^-\Sigma^+$ (**d**) second harmonic probe response after circularly polarized (σ^+) excitation at various pump energies. Due to the broad linewidth of the laser, pump energies from 1.61 to 1.71 eV overlap with the A-exciton resonance and yield similar exciton dynamics, although the time zero coherent artifact is modified.

Our results agree with recent tr-ARPES measurements of WS_2 monolayers which observed rapid room-temperature valley depolarization on 50 fs timescales[24,25]. While valley polarization lasting up to 10 ps has been observed in tr-ARPES[25], it is only possible through freezing out the IEC and phonon scattering at low pump fluences and temperatures <100 K to minimize the population of excitons with non-zero center of mass momentum[25]. Additional tr-ARPES studies at room temperature would be required to further resolve the origin of our observed ultrafast room temperature valley depolarization and distinguish between IEC, EY phonon scattering, and scattering through the Σ point.

Conclusion

Although the unique spin-valley locking and polarization of TMD monolayers have many proposed applications, a clear understanding of the competing inter- and intra-valley scattering rates is required. Our circularly polarized pump-probe time-resolved SH spectroscopy technique provides a straightforward method for resolving TMD valley dynamics with fs time resolution at the microscale. As demonstrated here with monolayer WSe_2, we identified separate spin- and momentum-forbidden scattering rates, resolvable simultaneously with a dual-polarization simultaneous detection scheme. This time-resolved pump-probe technique is easily extendable to other spin- or valley-polarized systems such as TMD heterostructures or Moiré lattices and other 2D material devices, allowing rapid characterization of ultrafast femtosecond processes with an all-optical technique.

Data availability

All relevant data is available from the corresponding author, Ulrich Höfer, upon request.

Received: 6 January 2026; Accepted: 31 July 2026;
Published online: 20 August 2026

References

1. Zhao, W. et al. Evolution of electronic structure in atomically thin sheets of ws2 and wse2. *ACS Nano* **7**, 791–797 (2013).
2. Chernikov, A. et al. Exciton binding energy and nonhydrogenic rydberg series in monolayer ws2. *Phys. Rev. Lett.* **113**, 076802 (2014).
3. Mak, K. F. & Shan, J. Photonics and optoelectronics of 2d semiconductor transition metal dichalcogenides. www.nature.com/naturephotonics (2016).
4. Baugher, B. W., Churchill, H. O., Yang, Y. & Jarillo-Herrero, P. Optoelectronic devices based on electrically tunable p-n diodes in a monolayer dichalcogenide. *Nat. Nanotechnol.* **9**, 262–267 (2014).
5. Shanks, D. N. et al. Nanoscale trapping of interlayer excitons in a 2d semiconductor heterostructure. *Nano Lett.* **21**, 5641–5647 (2021).
6. Tran, K. et al. Evidence for moiré excitons in van der Waals heterostructures. *Nature* **567**, 71–75 (2019).
7. Xu, X., Yao, W., Xiao, D. & Heinz, T. F. Spin and pseudospins in layered transition metal dichalcogenides. *Nat. Phys.* **10**, 343–350 (2014).
8. Glazov, M. M. et al. Exciton fine structure and spin decoherence in monolayers of transition metal dichalcogenides. *Phys. Rev. B* **89**, 201302 (2014).
9. Yu, T. & Wu, M. W. Valley depolarization due to intervalley and intravalley electron-hole exchange interactions in monolayer mos2. *Phys. Rev. B* **89**, 205303 (2014).
10. Yan, T., Qiao, X., Tan, P. & Zhang, X. Valley depolarization in monolayer WSe2. *Sci. Rep.* **5**, 15625 (2015).
11. Schmidt, R. et al. Ultrafast coulomb-induced intervalley coupling in atomically thin ws2. *Nano Lett.* **16**, 2945–2950 (2016).
12. Selig, M. et al. Ultrafast dynamics in monolayer transition metal dichalcogenides: Interplay of dark excitons, phonons, and intervalley exchange. *Phys. Rev. Res.* **1**, 022007 (2019).
13. Molina-Sánchez, A., Sangalli, D., Wirtz, L. & Marini, A. Ab initio calculations of ultrashort carrier dynamics in two-dimensional materials: valley depolarization in single-layer WSe2. *Nano Lett.* **17**, 4549–4555 (2017).
14. Wang, Z. et al. Intravalley spin-flip relaxation dynamics in single-layer ws2. *Nano Lett.* **18**, 6882–6891 (2018).
15. Selig, M. et al. Suppression of intervalley exchange coupling in the presence of momentum-dark states in transition metal dichalcogenides. *Phys. Rev. Res.* **2**, 023322 (2020).
16. Malic, E. et al. Dark excitons in transition metal dichalcogenides. *Phys. Rev. Mater.* **2**, 014002 (2018).
17. Mak, K. F., He, K., Shan, J. & Heinz, T. F. Control of valley polarization in monolayer mos2 by optical helicity. *Nat. Nanotechnol.* **7**, 494–498 (2012).
18. Zeng, H., Dai, J., Yao, W., Xiao, D. & Cui, X. Valley polarization in mos2 monolayers by optical pumping. *Nat. Nanotechnol.* **7**, 490–493 (2012).
19. Pogna, E. A. A. et al. Photo-induced bandgap renormalization governs the ultrafast response of single-layer mos2. *ACS Nano* **10**, 1182–1188 (2016).
20. Wang, G. et al. Giant enhancement of the optical second-harmonic emission of wse2 monolayers by laser excitation at exciton resonances. *Phys. Rev. Lett.* **114**, 097403 (2015).
21. Ho, Y. W. et al. Measuring valley polarization in two-dimensional materials with second-harmonic spectroscopy. *ACS Photonics* **7**, 925–931 (2020).
22. Zimmermann, J. E. et al. Ultrafast charge-transfer dynamics in twisted mos2/wse2 heterostructures. *ACS Nano* **15**, 14725–14731 (2021).
23. Zimmermann, J. E., Kim, Y. D., Hone, J. C., Höfer, U. & Mette, G. Directional ultrafast charge transfer in a WSe2/mose2 heterostructure selectively probed by time-resolved shg imaging microscopy. *Nanoscale Horiz.* **5**, 1603–1609 (2020).
24. Kunin, A. et al. Momentum-resolved exciton coupling and valley polarization dynamics in monolayer ws2. *Phys. Rev. Lett.* **130**, 046202 (2023).
25. Zhu, X. et al. A holistic view of the dynamics of long-lived valley polarized dark excitonic states in monolayer ws2. *Nat. Commun.* **16**, 6385 (2025).
26. Li, Y. et al. Measurement of the optical dielectric function of monolayer transition-metal dichalcogenides: Mos2, mose2, ws2, and wse2. *Phys. Rev. B* **90**, 205422 (2014).
27. Siday, T. et al. Ultrafast nanoscopy of high-density exciton phases in wse2. *Nano Lett.* **22**, 2561–2568 (2022).
28. Herrmann, P. et al. Nonlinear valley selection rules and all-optical probe of broken time-reversal symmetry in monolayer wse2. *Nat. Photonics* **19**, 300–306 (2025).
29. Fajardo, E. A. & Winkler, R. Effective dynamics of two-dimensional bloch electrons in external fields derived from symmetry. *Phys. Rev. B* **100**, 125301 (2019).
30. Cheng, J. et al. Chiral selection rules for multi-photon processes in two-dimensional honeycomb materials. *Opt. Lett.* **44**, 2141 (2019).
31. Zimmermann, J. E., Li, B., Hone, J. C., Höfer, U. & Mette, G. Second-harmonic imaging microscopy for time-resolved investigations of transition metal dichalcogenides. *J. Phys. Condens. Matter* **32**, 485901 (2020).
32. Perfetto, E., Wu, K. & Stefanucci, G. Theory of coherent phonons coupled to excitons. *npj 2D Mater. Appl.* **8**, 40 (2024).
33. Xiao, D., Liu, G.-B., Feng, W., Xu, X. & Yao, W. Coupled spin and valley physics in monolayers of mos2 and other group-vi dichalcogenides. *Phys. Rev. Lett.* **108**, 196802 (2012).
34. Cao, T. et al. Valley-selective circular dichroism of monolayer molybdenum disulphide. *Nat. Commun.* **3**, 887 (2012).
35. Glinka, Y. D., Tolk, N. H., Liu, X., Sasaki, Y. & Furdyna, J. K. Spatially resolved pump-probe second harmonic generation study of multilayer semiconductor heterostructures. *Appl. Phys. Lett.* **91**. https://pubs.aip.org/apl/article/91/23/231104/334415/Spatially-resolved-pump-probe-second-harmonic (2007).
36. Lu, X. & Srinivasan, K. Considering photoinduced second-harmonic generation as a dc Kerr optical parametric oscillation or amplification process. *Phys. Rev. Appl.* **16**, 014027 (2021).
37. Aktsipetrov, O. A. et al. dc-electric-field-induced and low-frequency electromodulation second-harmonic generation spectroscopy of Si (001) – SiO_2 interfaces. *Phys. Rev. B* **60**, 8924–8938 (1999).
38. Nelson, C. & Zhu, X.-Y. Determine electric field directions at semiconductor surfaces by femtosecond frequency domain interferometric second harmonic (fdish) generation. *Chem. Phys.* **478**, 69–72 (2016).
39. Wallauer, R. et al. Momentum-resolved observation of exciton formation dynamics in monolayer ws2. *Nano Lett.* **21**, 5867–5873 (2021).

Author contributions

M.A., G.M., J.G. and U.H. conceived and designed the experiments. M. A. prepared the samples and conducted the measurements. M.A., B.G.W., M.B.R. and U.H performed the data analysis and the modeling. B.G.W. wrote the manuscript with contributions from all authors.

Funding

Marleen Axt, Gerson Mette, Jens Güdde, and Ulrich Höfer acknowledge funding from the Deutsche Forschungsgemeinschaft (DFG, German Research Foundation), Project-ID223848855-SFB 1083. Benjamin G. Whetten and Markus B. Raschke acknowledge funding from the US Department of Energy, Office of Basic Sciences, Division of Material Sciences and Engineering, under award no. DESC0008807.

Competing interests

M.B.R. is an Editorial Board Member for Communications Physics but was not involved in the editorial review or peer review, nor in the decision to publish this article.

Additional information

Correspondence and requests for materials should be addressed to Markus B. Raschke or Ulrich Höfer.

Peer review information *Communications Physics* thanks Yinong Zhang and the other anonymous reviewer for their contribution to the peer review of this work.